

The Unique Carrier Mobility of Monolayer Janus MoSSe Nanoribbons: A First-Principles Study

Wen-Jin Yin^{1,2}, Yu Liu¹, Bo Wen², Xi-Bo Li³, Yi-Feng Chai¹, Xiao-Lin Wei⁴, Shangyi Ma^{5*}, and Gilberto Teobaldi^{6,7,8}

¹School of Physics and Electronic Science, Hunan University of Science and Technology, Xiangtan 411201, China

²Beijing Computational Science Research Center, Beijing 100084, China

³Department of Physics, Jinan University Guangzhou 510632, P. R. China

⁴Department of Physics and Laboratory for Quantum Engineering and Micro-Nano Energy Technology, Xiangtan University, Xiangtan 411105, Hunan, China

⁵Shenyang National Laboratory for Materials Science, Institute of Metal Research, Chinese Academy of Sciences, Shenyang 110016, China

⁶Scientific Computing Department, STFC UKRI, Rutherford Appleton Laboratory, Harwell Campus, OX11 0QX Didcot, United Kingdom

⁷Stephenson Institute for Renewable Energy, Department of Chemistry, University of Liverpool, L69 3BX Liverpool, United Kingdom

⁸School of Chemistry, University of Southampton, High Field, SO17 1BJ Southampton, United Kingdom

*Email: syma@imr.ac.cn

Abstract

Charge-carrier mobility is a determining factor for the transport properties of semiconductor materials, and strongly related to the opto-electronics performance of nanoscale devices. Here, we investigate the electronic properties and charge-carrier mobility of monolayer Janus MoSSe nanoribbons by means of first-principles simulations coupled with deformation potential theory. The simulations indicate that zigzag nanoribbons are metallic. Conversely, armchair nanoribbons are semiconducting and show oscillations in the calculated band-gap as a function of the edge-width according to a $3p < 3p+1 < 3p+2$ rule, with p being the integer number of repeat units along the non-periodic direction of the nanoribbon. Although the charge-carrier mobility of armchair nanoribbons oscillates with the edge-width, its magnitude is comparable to its two-dimensional sheet counterpart. A robust room-temperature carrier mobility is calculated for 3.5 nm armchair nanoribbons with values ranging from $50 \text{ cm}^2\text{V}^{-1}\text{s}^{-1}$ to $250 \text{ cm}^2\text{V}^{-1}\text{s}^{-1}$ for electrons (e) and holes (h), respectively. Comparison of these values with the results for periodic flat sheet (e: $73.8 \text{ cm}^2\text{V}^{-1}\text{s}^{-1}$; h: $157.2 \text{ cm}^2\text{V}^{-1}\text{s}^{-1}$) reveals enhanced (suppressed) hole (electron) mobility in the Janus MoSSe nanoribbons. This is opposite to what previously found for MoS₂ nanoribbons, namely larger mobility for electrons in comparison to holes. These differences are rationalized on the basis of the different structure, edge electronic states and deformation potentials present in the MoSSe nanoribbons. The present results provide guidelines for structural and electronic engineering of MoSSe nanoribbon edges towards tailored electron transport properties.

Introduction

Over the past decade, low dimensional materials have attracted substantial attention owing to their appealing physical and chemical properties such as large surface area, tunable band gap, and abundance of reactive sites.^[1-5] Graphene, as the archetypal two-dimensional material, presents excellent half-integer quantum hall effect, high migration rate, and mass-less charge-carrier transport properties.^[6, 7] However, the absence of a band gap in pristine graphene has limited its application in nanoscale electronic devices.^[6, 8, 9] This limitation has triggered extensive research in strategies to open the band gap of graphene. Structure tailoring such as formation of armchair and zigzag edges can be effective in controlling the electronic property of graphene. Unfortunately, the carrier mobility of graphene nanoribbons can be dramatically reduced by comparison to the pristine material due to the disappearance of the Dirac cone and scattering effects.^[10, 11] For example, characterization of sub-10 nm graphene nanoribbon field effect transistors has shown that the charge-carrier mobility drops to less than $200 \text{ cm}^2\text{V}^{-1}\text{s}^{-1}$ for the reduced widths needed to open a sufficiently large band gap in the systems.^[12, 13]

Searching for other low dimensional graphene-analog materials with intrinsic band gap has also been extensively pursued. Transition metal dichalcogenides (TMDs) as the typical graphene analogs, have received great interest due to their unique structural and electronic properties.^[14] By combining different chalcogens (e.g. S, Se and Te) and transition metal (e.g. Mo, W, Nb and V) atoms, various TMDs structures with tailored electronic properties have been obtained.^[15, 16] Monolayer MoS₂, a member of the TMDs family, is a semiconductor with band gap of about 1.9 eV.^[17] It has hence been regarded as a promising candidate for field effect transistor with an on/off ratio exceeding 10^8 .^[18] Characterization of suspended MoS₂ sheets reveals charge-carrier mobility in the range of $0.5\text{-}3 \text{ cm}^2\text{V}^{-1}\text{s}^{-1}$. However, the charge-carrier mobility of electrons and holes in the pristine MoS₂ is relatively low, leading to low performance in electronic devices.^[19-21] By improving sample quality, removing adsorbates, or depositing a high-dielectric layer, extrinsic scattering sites such as charged impurities and grain boundaries can be partially suppressed, leading to enhancement of charge-carrier mobility up to around $200 \text{ cm}^2\text{V}^{-1}\text{s}^{-1}$.^[22-25] Further computational results shows that the charge-carrier mobility in armchair MoS₂ nanoribbons is comparable to its sheet counterpart.^[26]

Formation of Janus structures has also been found to be effective in tailoring the physical properties of the systems.^[27-29] For example, **Guo** et al found that the Janus group III chalcogenide structures can greatly enhance the piezoelectric effect associated with the intrinsic dipole perpendicular to the plane structure.^[30] This dipole generates a built-in electric field, which in turn facilitates separation of photogenerated charge-carriers, to the benefit of photocatalytic reactivity.^[31, 32] Recently, **Lu** et al have grown a Janus monolayer of transition metal dichalcogenides, MoSSe, succeeding in breaking the out-of-plane structural symmetry of the single layer MoS₂.^[33] Theoretical results indicate that the charge-carrier mobility of monolayer Janus MoSSe structure is about $157 \text{ cm}^2\text{V}^{-1}\text{s}^{-1}$ and $74 \text{ cm}^2\text{V}^{-1}\text{s}^{-1}$ for holes and electrons, respectively. It is furthermore easily tunable by changing the layer thickness and resultant perpendicular dipole.^[34] Further HSE06 results by **Ma** et al. suggest that the Janus MoSSe sheet can be a

potential water splitting photocatalyst, with wide solar-absorption and retarded charge-carrier recombination.^[35] Prompted by these results, other studies on photocatalytic water splitting have emerged. Using non-collinear, screened-hybrid DFT (HSE06) simulations, **Din** *et al.* found that MoSSe/GeC heterostructures can present band alignment appropriate for visible light water splitting.^[36] In addition, **Guan** *et al.* found that few layer Janus MoSSe can also be suitable for visible light water splitting.^[25] In contrast to MoS₂, the band gap of MoSSe is about 1.66 eV (at PBE level), which is smaller than that of MoS₂ (1.78 eV, also at PBE level), suggesting a wider visible light absorption. Critically, owing to the Janus asymmetric structure not present in MoS₂, there is an intrinsic dipole moment perpendicular to the MoSSe plane. These properties combined point to MoSSe as a potentially promising candidate for infrared-visible light water splitting, nanoelectric devices, and piezoelectric applications.^[37-39] Regardless of the specific photocatalytic or electronic-device application, the Janus structure should be cut into nanoribbons to be usable in practical devices, which makes it imperative to understand and control the role of physical truncation and nanoribbon-edges for the opto-electronic properties of these systems, starting from their charge-carrier mobility.

To this end, the purpose of this work is to unveil the electronic properties of the Janus MoSSe nanoribbons. Towards definition of currently missing guidelines, we focus on the role of the edge-width for the emerging electronic structure and charge-carrier mobility of Janus MoSSe nanoribbons as well as on the atomistic and electronic factors governing charge-carrier mobility in these systems. The calculated results enable rationalization of the dependence of the nanoribbon's electronic structure and charge-carrier mobility on its edge-width. The simulations also indicate that the 1D charge-carrier mobility in armchair-truncated Janus MoSSe nanoribbons is comparable to that for 2D, flat MoSSe sheets, which anticipates expectedly robust charge-transport performance.

Computational Methods

All the simulations were carried out by density functional theory (DFT) as implemented in the Vienna ab initio simulation program package (VASP).^[40, 41] We used the Perdew-Burke-Ernzerhof (PBE) exchange-correlation functional, based on the generalized gradient approximation (GGA).^[42] The projector augmented wave (PAW) method was used to describe the atomic cores. The plane-wave energy cutoff was 500 eV, numerically checked to yield energies converged to within 0.001 eV/atom. The convergence criterion for the self-consistent DFT solution was 10⁻⁶ eV between two consecutive electronic steps. We used a 15×1×1 Monkhorst-Pack \mathbf{k} -point grid, with 15 \mathbf{k} -points along the periodic direction of the nanoribbons. A vacuum buffer of 15 Å was added to avoid interactions between adjacent images. The atomic structures were fully relaxed until the residual force was less than 0.001 eV/Å on each atom. van der Waals (vdW) interactions were accounted for at the DFT-D3 level.^[43]

The charge-carrier mobility in the one dimensional nanoribbons was estimated by the phonon-limited formula:^[26, 44, 45]

$$m = (e\hbar^2 C_{1D}) / [(2p k_b T)^{1/2} m^{2/3} E_i^2] \quad (1)$$

where e , \hbar , and k_b are the electron charge, the Planck constant, and the Boltzmann

constant, respectively. m^* is the effective mass along the transport direction (either m_x or m_y along the x or y direction, respectively). C_{ID} is the elastic modulus of the longitudinal acoustic mode in the propagation direction, which is defined as $C_{ID} = 2(E - E_0)/[l_0(\Delta L_i/L_i)^2]$. E and E_0 are the total energy of the system following deformation along the possible direction and at its equilibrium minimum-energy geometry, respectively. l_0 is the length of the one-dimensional nanoribbon at the equilibrium state. E_i is the deformation potential (DP) associated with phonon scattering, which can be calculated as: $E_i = \Delta E_i/(\Delta L_i/L_i)$. E_i is computed from the energy level change induced by the compression or expansion of the MoSSe nanoribbon by a $\Delta L_i/L_i = 0.005$ step in the transport direction. It should be mentioned that all the structures were fully relaxed regardless of deformation. The energy (E_i) of the valence band maximum (VBM) and conduction band minimum (CBM) is used for the hole (E_h) and electron (E_e), respectively. All the band edges are aligned to the vacuum energy level. To ensure the accuracy of our results, the PBE+SOC functional is used to check the basic electronic and carrier behavior of the Janus MoSSe armchair nanoribbons.

Results and Discussion

The Janus MoSSe sheet is a two-dimensional hexagonal structure with \mathbf{a}_h and \mathbf{b}_h primitive cell vectors, see **Fig. 1(a)**. The primitive cell contains three atoms vertically displaced in three different atomic-layers, see **Fig. 1(b)**. The atomic species are Mo, S, and Se. The Mo atoms are six-fold coordinated, whereas the S and Se atoms are three-fold coordinated. The Janus MoSSe monolayer can also be described via an orthogonal supercell defined by the \mathbf{a}_o and \mathbf{b}_o vectors, see **Fig. 1(a)**. The supercell built in this way allows for a more direct quantification of the charge-carrier mobility along the zigzag (\mathbf{a}_o) and armchair (\mathbf{b}_o) directions. The optimized structural parameters for the periodic MoSSe sheet are $\mathbf{a}_h = \mathbf{b}_h = 3.21$ Å. The Mo-S bond length is about 2.41 Å, and the Mo-Se bond is about 2.52 Å long. The $\angle\text{MoSMo}$ angle in the MoSSe sheet is about 83.72° , while the $\angle\text{MoSeMo}$ angle is about 79.08° i.e., smaller than the $\angle\text{MoSMo}$ one. This may be attributed to the larger radii and lower oxidation of the Se atoms. As previously shown, such asymmetric structure tailoring can be effective in inducing novel emerging properties in low-dimensional materials.^[46, 47] Similar to hexagonal 2D materials such as graphene and MoS₂, the MoSSe sheet can also be patterned into two types of nanoribbons depending on the cutting direction. These are armchair (edges parallel to \mathbf{b}_o) and zigzag (edges parallel to \mathbf{a}_o) nanoribbons. The atomic structure of the armchair and zigzag MoSSe nanoribbons are shown in **Fig. 1(c)**. The width of the armchair/zigzag nanoribbon is defined by N_a/N_z that counts the number of the repeating units in the nanoribbon model (along the non-periodic in-plane direction), see **Fig. 1(c)**. In the following, we focus on armchair nanoribbons with N_a ranging from 6 to 22 (3.5 nm width). As for the zigzag nanoribbons, we mainly focus on models with N_z ranging from 6 to 11 due to the metallic property. After relaxation, we find that the Mo-S and Mo-Se bonds at the edges are different from those at the innermost part of the nanoribbon. The Mo-S and Mo-Se bonds at edge are about 0.01 and 0.05 Å larger than those at innermost part of the nanoribbon.

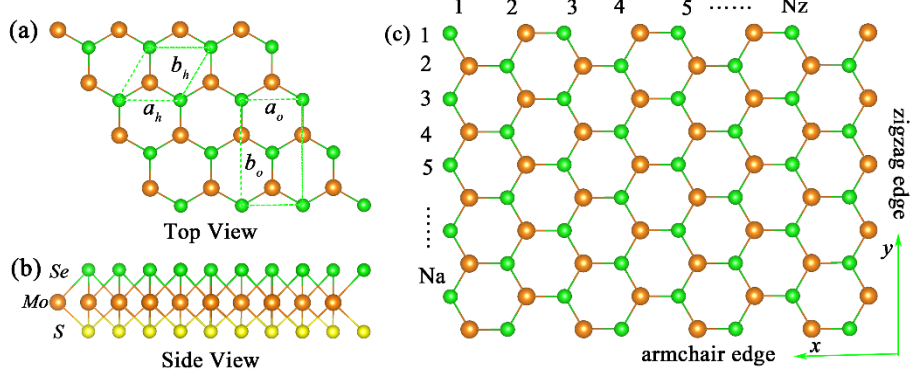


Figure 1. (Color online) Atomic structure model of the monolayer Janus MoSSe sheet and Nanoribbons. (a) Top view of the MoSSe monolayer sheet. The dashed lines represent the hexagonal primitive cell (defined by a_h and b_h) and the orthogonal supercell (defined by a_o and b_o). (b) Side view of the MoSSe monolayer sheet with three atomic-layers (upper Se atom, middle Mo atom, and lower S atom). (c) Atomic structure and labeling used for the Janus MoSSe nanoribbons. The armchair (zigzag) nanoribbons are periodic along the x (y) direction. The golden, yellow, and light green balls are Mo, S, and Se atoms, respectively.

Table 1. The relaxed lattice and structural parameters (bond lengths and bond angles) for the Janus MoSSe monolayer sheet and its nanoribbons.

System	Lattice parameter		Bond length (Å)		Angle (degree)		
	a_o	b_o	Mo-S	Mo-Se	$\angle MoSMo$	$\angle SMoS$	$\angle MoSeMo$
Sheet	3.21	5.57	2.41	2.52	83.72^0	82.28^0	79.08^0
armchair		5.55	2.42	2.57	86.14^0	82.45^0	80.86^0
zigzag	3.20		2.38	2.53	83.77^0	81.48^0	81.21^0

It has been reported that Janus MoSSe sheets are direct-gap semiconductors with a band gap of about 1.66 eV.^[34] The corresponding electron carrier mobility is about 73.8 cm²V⁻¹s⁻¹, and the hole carrier mobility is about 157.2 cm²V⁻¹s⁻¹. The larger hole mobility for monolayer sheet originates from the smaller deformation potential (E_h) of the valence band compared with that of the conduction band (E_e). In addition, there exists an intrinsic dipole of about 0.037 $e \cdot \text{\AA}$, perpendicular to the two-dimensional periodic plane of the sheet.

Structure tailoring can induce novel emerging properties in low-dimensional materials.^[46, 47] It has been reported that the zero-band gap in graphene can be opened to up 0.5 eV in nanoribbons^[48], and that the carrier mobility of graphene nanoribbons can be dramatically reduced to less than 200 cm²V⁻¹s⁻¹.^[13] In addition, MoS₂ zigzag nanoribbons are metallic, irrespective of the edge-width and nanoribbon thickness. Conversely, MoS₂ armchair nanoribbons are semiconductors, and their band gaps converge to a value of \sim 0.56 eV as the edge-width increases.^[49] We accordingly start

our study by analyzing and quantifying the role of the armchair or zigzag edges for the electronic properties of the Janus MoSSe nanoribbons. The simulations indicate that, regardless of the nanoribbon width, the systems with zigzag edges are metallic, see **Fig. S1** in the Supporting Information (**SI**). Conversely, and again regardless of the width of the nanoribbon, we find the systems with armchair edges to be semiconducting (**Fig. 2**), as the pristine Janus MoSSe sheet. However, the magnitude of the band gap for the armchair nanoribbons and monolayer sheet is quite different. Although the band gap of the armchair nanoribbon changes from 0.37 eV to 0.495 eV with increasing edge-width, they remain considerably smaller than what calculated at the same level of theory for the periodic sheet (1.66 eV).

Further analysis of the results reveal that the band gap of the zigzag nanoribbons oscillates with the edge-width. For the system considered, the edge-width can be classified into three families, namely $N_a = 3p$, $3p+1$, and $3p+2$, with p being an integer number ($2 < p < 8$ for the size of the systems studied). When the armchair edge $N_a=3p$, the band gap gradually increases from 0.37 eV to 0.48 eV, plateauing to 0.495 eV for $N_a=22$. The results for the $N_a=3p+1$ and $N_a=3p+2$ models follow a qualitatively similar rate of increase with N_a converging to the 0.49 eV values for the larger models. As seen in **Fig. 2**, we find the calculated band-gap to follow a $3p < 3p+1 < 3p+2$ trend, regardless of the value of p . This variation rule is quite similar to the case of MoS₂, where the band gaps of armchair nanoribbons converge to a value of ~ 0.56 eV, smaller than the band gap of its sheet (~ 1.9 eV).^[49] In addition, both MoS₂ and MoSSe sheets have been prepared successfully in recent years. It has been reported that MoS₂ nanoribbons can be fabricated by scanning probe lithography^[50], and that MoSSe may own some similarities with MoS₂. On the other hand, DFT calculations can access the band gaps of different semiconductors, and the corresponding changes going from two-dimensional periodic systems to nanoribbons (as for MoS₂). We thus believe our results can provide guidance for further experiments to quantify the sheet to nanoribbons changes in MoSSe. To the best of our knowledge, these experiments are yet to appear in the literature. To check the effect of SOC on the band gap, we examined the electronic properties of the armchair nanoribbons at PBE+SOC level. To quantify the SOC effect, the electronic structure of the Janus MoSSe sheet is firstly studied. The calculated results show that the SOC-induced band splitting at the VBM is more prominent than that at the CBM (**Fig. S2**), consistent with previous results^[51]. These results indicate a non-negligible effect of SOC on the band-structure of the Janus MoSSe sheet. **Fig. S3** reports the PBE and PBE+SOC band gap of the armchair nanoribbons. It can be found that the band gaps calculated at PBE+SOC level are close (to within 0.1 eV) to the PBE results. Notably, also at PBE+SOC level, the value of the band gap also changes as a function of the edge width according to a $3p < 3p+1 < 3p+2$ rule, as for the PBE case. In addition, the dipole moment of the systems appears width dependent as shown in **Fig. S4**. The dipole moment is linearly increasing for $0.18 \text{ e} \cdot \text{\AA}$ ($N_a=9$) to $0.46 \text{ e} \cdot \text{\AA}$ ($N_a=19$). The corresponding value in per width is $0.02 \text{ e} \cdot \text{\AA}$ ($N_a=6$) and $0.024 \text{ e} \cdot \text{\AA}$ ($N_a=19$). These results indicate that modifications in the width of the MoSSe armchair nanoribbons, a form of structure tailoring, can be effective in modifying their electronic structure starting from the band-gap, thus allowing tailoring of electronic properties. In

the following we quantify the effect of these changes on the systems' charge-carrier mobility.

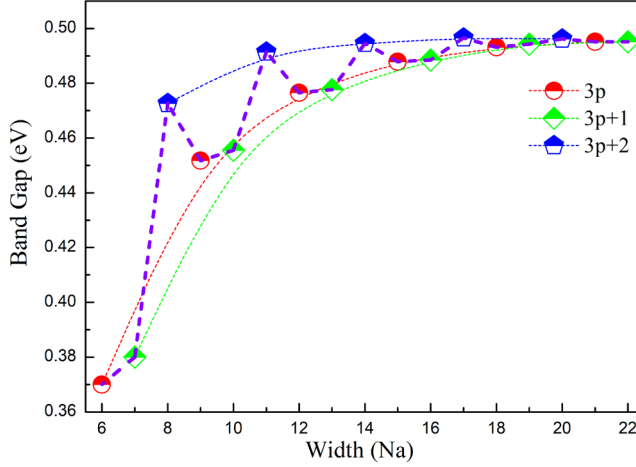


Figure 2. (Color online) Calculated band gap of the armchair MoSSe nanoribbons as a function of the edge-width (N_a). The widths modeled can be divided into three $N_a = 3p$, $3p+1$, and $3p+2$ families, with p being an integer value ($2 < p < 8$ in this study).

Analysis of the electronic properties of the armchair MoSSe nanoribbons is expanded by considering the calculated band structure and atom-projected band-densities, shown in **Fig. 3**. We limit this analysis to a subset of the systems studied, namely the $N_a=9$, 10 and 11 (armchair) nanoribbons. The calculated band-gaps for these systems are 0.45 eV, 0.46 eV and 0.49 eV, respectively. The simulations indicate that, for all the three systems, the valence band minimum (VBM) is located at the Γ -point. In contrast, the conduction band maximum (CBM) is located roughly at the center of the Γ -M path. Thus, all the three MoSSe nanoribbons turn out to be indirect-gap semiconductors. This is different from the results for monolayer MoSSe sheets, which instead point to a direct-gap semiconductor with both the CBM and VBM located at K-point.^[34] **Fig. 3** reports also the total and atom-projected Density of States for three MoSSe nanoribbons. The simulations indicate the CBM is mainly due to $3d$ Mo-states. In contrast, the VBM is characterized by strong electronic hybridization and mixing between $3d$ Mo, $3p$ S, and $4p$ Se states.

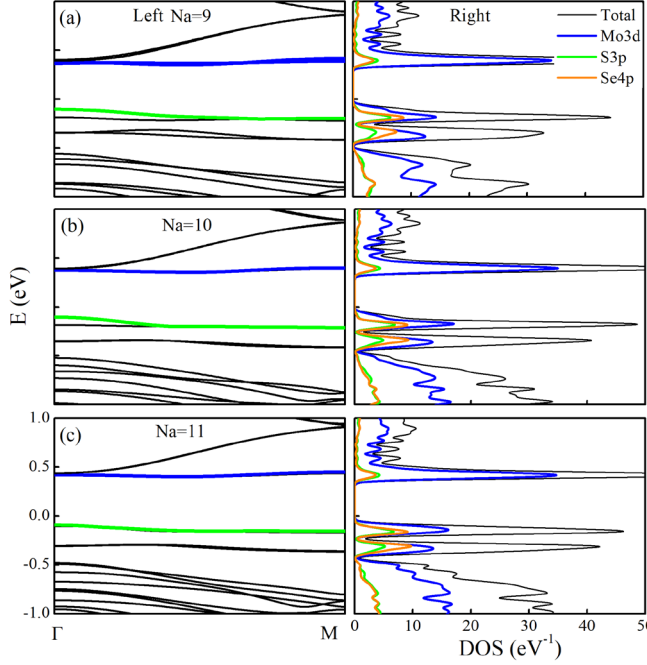


Figure 3. (Color online) Calculated band structure (left panels) with total and atom-projected density of states (right panels) for the armchair MoSSe nanoribbons. (a) $N_a=9$, (b) $N_a=10$, and (c) $N_a=11$. In the left panels, green and blue highlighting has been used for the first valence/conduction band under/above the Fermi level (0 eV).

Overall, these results show that both the band gap and the intrinsic vertical dipole moment can be non-negligibly tuned (>0.1 eV and < 0.01 $e \cdot \text{\AA}$ per width) by altering the width of the MoSSe nanoribbon. In the following, we quantify to extent to which the charge-carrier mobility is affected by the width of the nanoribbon. We recall that whereas graphene nanoribbons show a dramatically decreased charge-carrier mobility with respect to graphene sheets,^[52] the charge-carrier mobility of MoS₂ sheets and nanoribbons is comparable.^[49] Given the occurrence in Janus MoSSe nanoribbons of a perpendicular electrostatic dipole dependent on the edge-width (not present in MoS₂), we next quantify its role for the system's carrier mobility.

Fig. 4 reports the calculated elastic moduli (C_{1D}), carrier effective mass, deformation potential (DP), and carrier mobility for both electrons and holes in the armchair MoSSe nanoribbons as a function of the edge-width, as measured by N_a . Here, we only consider edge-widths between $N_a=6$ and $N_a=18$. This choice stems from realization that larger nanoribbons show convergence of the calculated band-gap (Fig. 2), which in turn suggests reasonably converged charge-carrier mobility properties too. The calculated elastic modulus (C_{1D}) for the $N_a=6$ nanoribbon is about 0.38×10^{12} eV/m (**Fig. 4a**). As the edge-width increases, C_{1D} also increases (effectively linearly), reaching values of 1.2×10^{12} eV/m for $N_a=13$, after which a different regime of increase is observed for N_a ranging from 14 to 18. The calculated increase of C_{1D} with the nanoribbon width is in line with earlier results for MoS₂ systems.^[49]

Besides the elastic moduli, the effective mass is another crucial factor for charge-carrier mobility (Eq. 1). As seen in **Fig. 4b**, and due to the different curvature of the VBM and CBM (**Fig. 3**), the differently sized MoSSe armchair nanoribbons display

quite different effective electron and hole masses. We find the electron effective mass to be about $1.22 m_0$ ($N_a=6$) i.e. over 2 times larger than for the flat, periodic MoSSe sheet ($0.6 m_0$). As the edge-width increases, the electron effective mass gradually increases to a maximum value of $4.5 m_0$ for $N_a=11$. Then it gradually reduces, converging to $3.7 m_0$ for edge-widths larger than $N_a=13$. These results indicate that edge tailoring of MoSSe nanoribbons leads to larger effective masses for the electron than for the flat (MoSSe) sheet, which is detrimental to carrier mobility.

The results for the hole are substantially different from those for the electron. The calculated hole effective mass (m_h) shows marked oscillations as a function of the nanoribbon edge-width (**Fig. 4b**). As for the band-gap (**Fig. 2**), also the calculated hole effective masses can be separated into three classes depending on the edge-width. Different trends are observed for the nanoribbons having edge-widths of $3p$, $3p+1$, and $3p+2$ (p is again an integer value). Starting with the $3p$ group, following a sudden decrease from $N_a=6$ ($3.5 m_0$) to $N_a=9$ ($1.9 m_0$), the hole effective mass converges to values of $1.7 m_0$ for $N_a>12$. Like the $3p$ case, also the hole effective mass for the $3p+1$ group increases with the edge-width, going from $1.1 m_0$ for $N_a=7$ to converged values of $1.5 m_0$ as $N_a>16$. The effective mass of the $3p+2$ group also increases with the edge-width, albeit with a different rate of change from the $3p$ and $3p+1$ groups. The calculated values increase from $1.22 m_0$ ($N_a=9$) to $1.8 m_0$ ($N_a>17$). In contrast to the trends observed for the band-gap ($3p<3p+1<3p+2$ in **Fig. 2**), the calculated hole effective mass follow a different relationship, namely $3p>3p+1>3p+2$. Comparison of the calculated hole effective mass for the nanoribbons (consistently $> 1.1 m_0$ in absolute value, **Fig. 4b**) and for the flat, periodic sheet ($0.73 m_0$) indicates that edge tailoring of MoSSe nanoribbons leads to larger effective masses for the hole than for the flat (MoSSe) sheet, which is detrimental to carrier mobility. Finally, as also seen in **Fig. 4b**, the (absolute value) of the effective mass for the hole is substantially (up to a factor of roughly 2) smaller than for the electron. As we discuss below, this result can be explained by the different symmetry of the frontier orbitals constituting the VBM and CBM.

Being related to the intensity of phonon scattering and its effects on the charge transport,^[53] the deformation potential (DP) can also strongly affect charge-carrier mobility. **Figs.4c-d** reports the calculated hole and electron DP for the nanoribbons studied. Also, DP displays oscillations with the edge-width of the nanoribbons. For the electron, DP oscillates between values of -1 eV and -4 eV in the $N_a=6-18$ range. The only exception to this trend is markedly more negative value of -7 eV for the DP of the $N_a=11$ nanoribbon. Similar to the results for the hole effective mass, also the calculated DP values for the electron follow a $3p<3p+1>3p+2$ trend, the only exception being the data for $N_a=9$ and $N_a=10$. Compared to the results for the electron, the hole DP show more contained variations as it changes between -0.5 eV and -2 eV in the $N_a=6-18$ range. Also in this case, the results for $N_a=11$ partially deviate with markedly decreased DP value of -3.2 eV. As the edge-width of the nanoribbon increases, the calculated DP values converge to -2.5 eV and -1.5 eV for the electron and hole, respectively. To check the SOC effect on the effective mass and DP, these were re-calculated at PBE+SOC level for the armchair nanoribbons with edge-width ranging from $N_a=6$ to $N_a=11$. **Fig.**

S5 and **Fig. S6** report the corresponding results. It can be seen that the effective mass and DP constant calculated by the PBE+SOC functional are quite close to the result calculated by the PBE functional, validating the reliability of the PBE results.

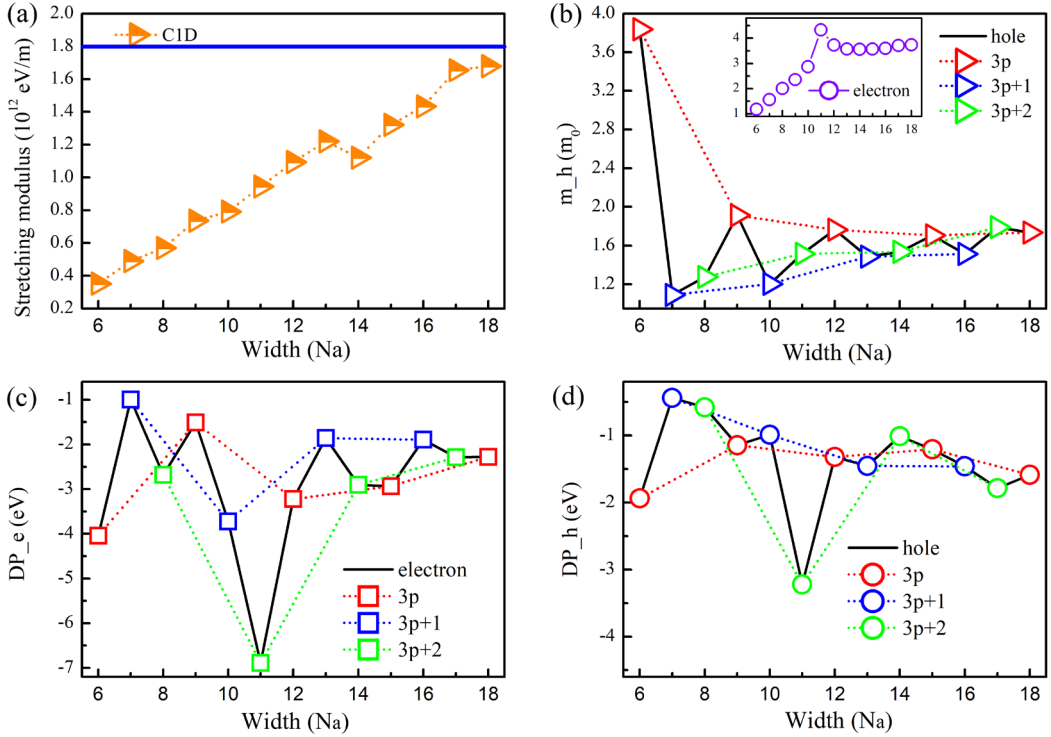


Figure 4. (Color online) Calculated (a) elastic modulus of the longitudinal acoustic mode in the propagation direction (C_{ID}), (b) electron (m_e) and hole (m_h) effective mass, and deformation potential (DP_e , h) for electrons (c) and holes (d). The blue horizontal line in panel (a) marks the C_{ID} value for the fully periodic MoSSe sheet.

Eq. (1) enables approximation of the room-temperature charge-carrier mobility for the Janus MoSSe nanoribbons based on the observables reported in **Fig. 4**. **Fig. 5** shows the calculated charge-carrier mobility for the systems studied. Both the electron and hole mobility oscillate with the edge-width. Both the electron and hole mobility are found to follow a $\mu_{3p} < \mu_{3p+1} > \mu_{3p+2}$ trend. As the edge-width of the nanoribbon is increased, the electron mobility plateaus to the value of about $48 \text{ cm}^2\text{V}^{-1}\text{s}^{-1}$. The calculated hole mobility of the largest nanoribbons instead converges to values of about $300 \text{ cm}^2\text{V}^{-1}\text{s}^{-1}$. To check the accuracy of the PBE results, the PBE+SOC functional is used to examine the carrier mobility of the Janus MoSSe armchair nanoribbons ($N_a=6-11$), as shown in **Fig. S7**. Critically, the PBE and PBE+SOC results for carrier mobility are in semi-quantitative agreement, with the largest deviations being observed for the $N_a=7$ and 8 nanoribbons (**Fig. S7**). Also importantly, both the PBE and PBE+SOC traces display the same qualitative dependence of the calculated carrier mobility on the edge-width (N_a in **Fig. S7**). Therefore, we are to conclude that the PBE+SOC results are in semi-quantitative agreement with the PBE ones, validating the reliability of our calculations in the manuscript. Thus, we find the hole mobility to be substantially (over six times) larger than the electron one. We attribute this result to the much lower hole-DP and to the generally smaller effective mass of the hole with respect to that of the electron (**Fig. 4**), with both terms appearing at the denominator of Eq. (1).

Comparison of the nanoribbons results with those for the flat Janus MoSSe periodic sheet (black dotted lines in **Fig. 5**) enables further considerations. Here, it should be mentioned that the calculated carrier mobility of the Janus MoSSe sheets along the zigzag- and armchair-directions is found to be the same. This result indicates isotropic carrier mobility in the Janus MoSSe sheets, consistent with previous results.^[34, 54] Apart from the $N_a=7$ case ($200 \text{ cm}^2\text{V}^{-1}\text{s}^{-1}$), the electron mobility of the nanoribbons is systematically lower than for the flat, periodic sheet. In contrast, the hole mobility of the nanoribbons for the whole range of edge-width studied turns out to be either comparable or larger than for the flat MoSSe sheet. This scenario is completely different from previous results of dramatically reduced carrier mobility for graphene nanoribbons by comparison to sheets.^[52]

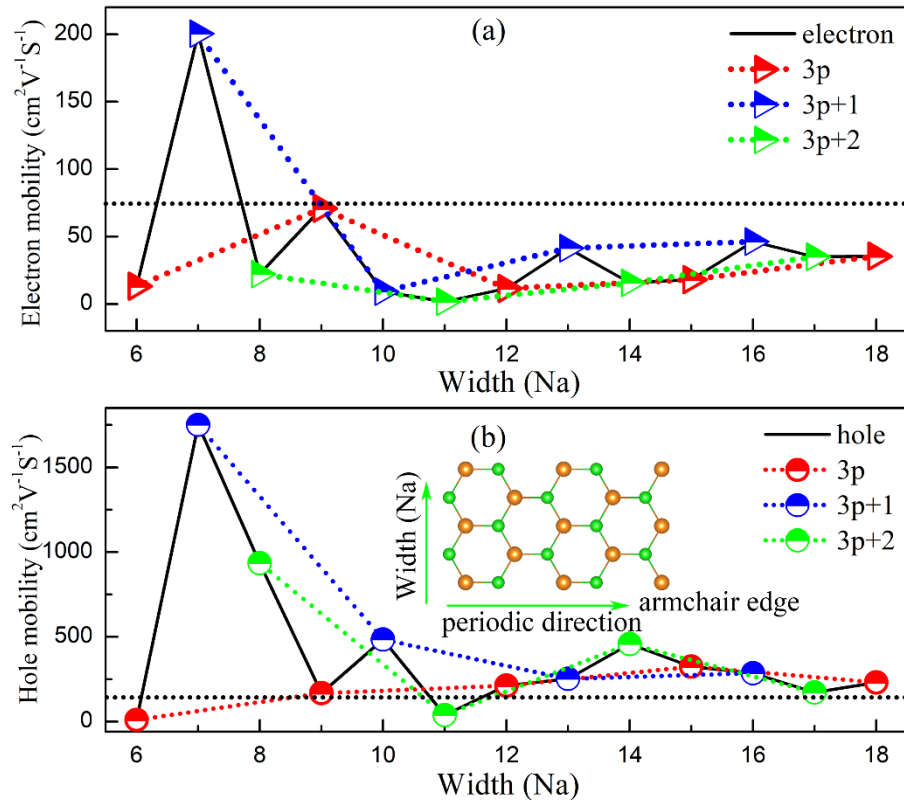


Figure 5. (Color online) Calculated charge-carrier mobility of the Janus MoSSe nanoribbons as a function of the edge-width. (a) Electron mobility, (b) Hole mobility. The charge-carrier mobility of the periodic, Janus MoSSe sheet is shown in both panels (black dotted line) for comparison.

We next analyze the origin of the different carrier mobility for the Janus MoSSe nanoribbons and sheet, focusing on the $N_a=8$ system. The effective mass (m^*) and deformation potential ($DP = E_i$) for the electron/hole in the nanoribbon are about 3.33/1.75 and 0.26/0.12 times larger than for the sheet, respectively. The larger effective mass originates from the relatively localized edge states seen **Fig. 6**, showing reduced dispersion in reciprocal space (**Fig. 3**), and leading to quantum size effects. On the other hand, the elastic modulus (C_{1D}) in nanoribbons at $N_a=8$ is 45 J/m^2 , which is smaller than for MoSSe sheet (136 J/m^2), due to the smaller size of the nanoribbon. As the charge-carrier mobility is directly proportional to C_{1D} and inversely proportional to

(powers of) m^* and E_i in Eq. 1, altogether the changes in C_{1D} , m^* and E_i leads to (0.31 times) lower electron mobility and (5.9 times) larger hole mobility in the nanoribbons with respect to the monolayer MoSSe sheet.

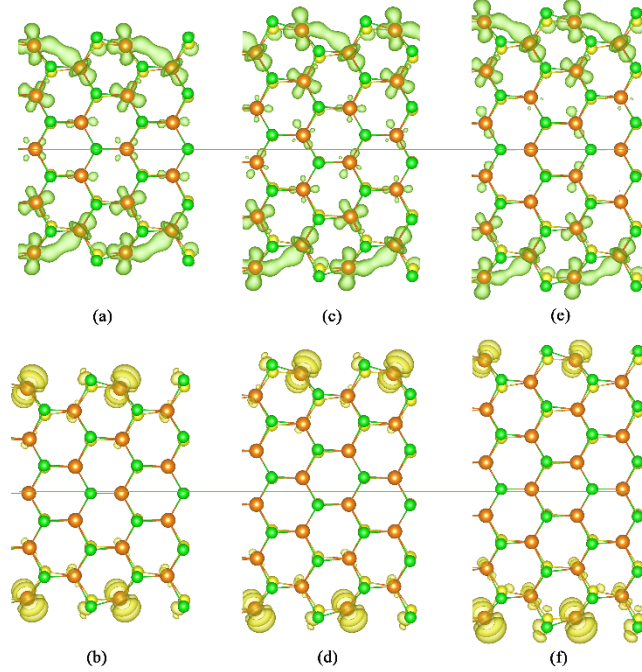


Figure 6. (Color online) Top view of the CBM (top panels) and VBM (bottom panels) charge-density (0.01 e bohr^{-3}) for the Janus MoSSe Nanoribbons of different edge-width. (a-b) $N_a=6$, (c-d) $N_a=7$, (e-f) $N_a=8$. The green horizontal line marks the longitudinal direction of the nanoribbon (i.e., the direction of stretching and charge-carrier transport).

As discussed above, the different carrier mobility for 1D Janus MoSSe nanoribbons and 2D sheet can be primarily attributed to the different effective mass (m^*) and deformation potential ($DP=E_i$). We next analyze the origin of the differences between the electron and hole mobility for the same nanoribbon. Once again, we focus on the $N_a=8$ system for this analysis. For this system, the hole mobility is about 42.5 times larger than the electron mobility. The hole effective mass and deformation potential are 0.64 and 0.22 times those of the electron. On this basis, and according to Eq. (1), it follows that higher mobility for holes is mainly due to their smaller DP with respect to electrons.

To further explain the reason, we turned to the wave functions of the band-edge state at the Γ point, which are equivalent to the frontier molecular orbitals [i.e., the highest occupied molecular orbital (VBM) for the hole and the lowest unoccupied molecular orbital (CBM) for the electron] responsible for transport. These are shown in **Fig. 6** for $N_a=6\sim 8$. The green horizontal line marks the longitudinal direction of the nanoribbon (i.e., the direction of stretching and charge-carrier transport). The real-space modulation of the CBM and VBM offers insights into the origin of their different deformation potential. The charge-density of the CBM is mainly localized at the Mo atoms in the nanoribbons. As shown in **Fig. 6(a), 6(c) and 6(e)**, the CBM-density decreases going from the edge to the center of the nanoribbon along the stretching axis. The real-space

distribution of the VBM is markedly different. The VBM charge-density is mainly localized at the Mo atom along the armchair edge, as shown in **Fig. 6(b), 6(d) and 6(e)**. It is therefore reasonable to expect that the localized CBM (electron state) is scattered more strongly by the acoustic phonon than the VBM (hole state). Thus, as the structure deformation responsible for the electron (E_e) and hole (E_h) deformation potential occurs along the edge direction, larger electrostatic interactions for the CBM than for the VBM will result in larger E_e values with respect to E_h ones, for an accordingly increased (reduced) hole (electron) mobility.

We finally turn to the origin of the different charge-carrier mobility for differently sized nanoribbons. It is known that the charge-carrier mobility of MoS_2 nanoribbons shows a 3p, 3p+1, and 3p+2 rule due to the edge states.^[49] Similar to MoS_2 , also the carrier mobility of Janus MoSSe nanoribbons is strongly affected by the edge states. The 3p+1 family, which has the smallest effective mass and the largest mobility, shows an A1 character in space group. The 3p and 3p+2 families have a B1 character in space group.^[49] The marked oscillatory behavior of the effective mass and mobility can thus be attributed to the different symmetry of the edge states, which results in different carrier-phonon coupling. Thus, the spatial distribution and orbital composition of the edge states in the MoSSe nanoribbons dominate the carrier mobility. Here, we take the $N_a=6$, 7, and 8 nanoribbons as representatives of the 3p, 3p+1, and 3p+2 groups, respectively. As seen in **Fig. 6**, the electron is localized at the Mo atoms across the whole $N_a=6$ nanoribbon. For $N_a=7$, the CBM charge-density is still localized on the Mo atoms but progressively decays from the edges towards the innermost region of the nanoribbon. In contrast with this trend, the CBM charge-density at the core of the $N_a=8$ nanoribbon is larger than for the $N_a=7$ one. Thus, as the structure deformation occurs, the electron deformation potential in these three nanoribbons follows an $E_e(N_a=6) > E_e(N_a=7) < E_e(N_a=8)$ trend, reflected in the emerging electron carrier mobility (μ): $\mu(N_a=6) > \mu(N_a=7) < \mu(N_a=8)$. Thus, based on the deformation potential and structure symmetry, the carrier mobility of the nanoribbons appear to follow a 3p rule with 3p<3p+1>3p+2.

Conclusions

In summary, we have investigated the structural, electronic, and carrier mobility properties of monolayer Janus MoSSe nanoribbons using first-principles calculations and deformation potential theory. It is shown that nanoribbons with zigzag edges are metallic, whereas those with armchair edges are semiconducting. The calculated band-gap for armchair nanoribbons follows a 3p<3p+1<3p+2 rule, with p being the integer number of repeat units along the non-periodic direction of the nanoribbon. Robust room-temperature carrier mobility (μ) is observed in the armchair MoSSe nanoribbons, with hole and electron mobility as large as $250 \text{ cm}^2\text{V}^{-1}\text{s}^{-1}$ and $50 \text{ cm}^2\text{V}^{-1}\text{s}^{-1}$, respectively. Comparison of these results with the mobility calculated for the flat sheet [h: $157.2 \text{ cm}^2\text{V}^{-1}\text{s}^{-1}$; e: $73.8 \text{ cm}^2\text{V}^{-1}\text{s}^{-1}$] indicates that Janus MoSSe nanoribbons have larger hole mobility, but smaller electron mobility, than flat MoSSe sheets. These results are the opposite than what found for MoS_2 nanoribbons that instead show larger mobility of electrons than for holes. The carrier mobility of Janus MoSSe nanoribbons oscillates with the edge-width, following a $\mu_{3p} < \mu_{3p+1} > \mu_{3p+2}$ rule. The unique carrier mobility is

attributed to the different VBM and CBM edge states, and ensuing deformation potential, present in MoSSe Nanoribbons. Our study suggests that structure tailoring together with edge engineering can provide effective routes to tailoring of transport properties in MoSSe nanostructures.

Acknowledgments

This work was supported by the Science Challenge Project (TZ2018004), the National Natural Science Foundation of China (Nos. 51572016, U1530401, 11704116, 11804090, 51472209, 11774298, U1401241, and 21503012), the Natural Science Foundation of Hunan Province, China (Grant No. 2019JJ50175 and 2019JJ50148). This research was also supported by a Tianhe-2JK computing time award at the Beijing Computational Science Research Center (CSRC). G. T. acknowledge also support by the Royal Society Newton Advanced Fellowship scheme (grant No. NAF\R1\180242).

References

- [1] P. Miro, M. Ghorbani-Asl, and T. Heine, *Angew Chem Int Ed Engl* **53**, 3015 (2014).
- [2] Z. Tan, et al., *Journal of the American Chemical Society* **138**, 16612 (2016).
- [3] R. Li, L. Zhang, L. Shi, and P. Wang, *ACS nano* **11**, 3752 (2017).
- [4] F. Shayeganfar, K. S. Vasu, R. R. Nair, F. M. Peeters, and M. Neek-Amal, *Physical Review B* **95**, 144109 (2017).
- [5] W. J. Ong, L. L. Tan, Y. H. Ng, S. T. Yong, and S. P. Chai, *Chemical Reviews* **116**, 7159 (2016).
- [6] M. Wang, Y. Pang, D. Y. Liu, S. H. Zheng, and Q. L. Song, *Computational Materials Science* **146**, 240 (2018).
- [7] X. T. Cui Jin, Xin Tan, Sean C. Smith, Ying Dai, and Liangzhi Kou, *Journal of Materials Chemistry A* **7**, 1099 (2019).
- [8] A. K. Geim, *Science* **324**, 1530 (2009).
- [9] K. S. Novoselov, A. K. Geim, S. V. Morozov, D. Jiang, Y. Zhang, S. V. Dubonos, I. V. Grigorieva, and A. A. Firsov, *Science* **306**, 666 (2004).
- [10] C. Lin, D. Shin, and A. A. Demkov, *Journal of Applied Physics* **117**, 225703 (2015).
- [11] Z.-K. Han, Y.-Z. Yang, B. Zhu, M. V. Ganduglia-Pirovano, and Y. Gao, *Physical Review Materials* **2** (2018).
- [12] T. Umebayashi, T. Yamaki, H. Itoh, and K. Asai, *Journal of Physics and Chemistry of Solids* **63**, 1909 (2002).
- [13] X. Wang, Y. Ouyang, X. Li, H. Wang, J. Guo, and H. Dai, *Physical Review Letters* **100**, 206803 (2008).
- [14] Y.-N. Z. Hui Zhang, Hao Liu and Li-Min Liu, *J. Mater. Chem. A* **2**, 15389 (2014).
- [15] M. Chhowalla, H. S. Shin, G. Eda, L.-J. Li, K. P. Loh, and H. Zhang, *Nat Chem* **5**, 263 (2013).
- [16] C. Ataca, H. Sahin, and S. Ciraci, *The Journal of Physical Chemistry C* **116**, 8983 (2012).
- [17] Q. Xiang, J. Yu, and M. Jaroniec, *Journal of the American Chemical Society* **134**, 6575 (2012).
- [18] B. Radisavljevic and A. Kis, *Nature Materials* **12**, 815 (2013).
- [19] S. Fathipour, et al., *Applied Physics Letters* **105**, 192101 (2014).
- [20] RadisavljevicB, RadenovicA, BrivioJ, GiacomettiV, and KisA, *Nat Nano* **6**, 147 (2011).
- [21] W. S. Yun, S. W. Han, S. C. Hong, I. G. Kim, and J. D. Lee, *Physical Review B* **85**, 033305 (2012).
- [22] G. Mattioli, F. Filippone, P. Alippi, and A. Amore Bonapasta, *Physical Review B* **78**, 241201(R) (2008).

- [23]S. Najmaei, et al., *Nature materials* **12**, 754 (2013).
- [24]X. Ma, X. Wu, H. Wang, and Y. Wang, *Journal of Materials Chemistry A* **6**, 2295 (2018).
- [25]R. Chaurasiya and A. Dixit, *Applied Surface Science* **490**, 204 (2019).
- [26]H. Cheng and A. Selloni, *The Journal of Chemical Physics* **131**, 054703 (2009).
- [27]K.-A. N. Duerloo, M. T. Ong, and E. J. Reed, *The Journal of Physical Chemistry Letters* **3**, 2871 (2012).
- [28]L. Dong, J. Lou, and V. B. Shenoy, *ACS Nano* **11**, 8242 (2017).
- [29]X. Gao, Y. Shen, Y. Ma, S. Wu, and Z. Zhou, *Inorganic Chemistry* **58**, 12053 (2019).
- [30]Y. Guo, S. Zhou, Y. Bai, and J. Zhao, *Applied Physics Letters* **110**, 163102 (2017).
- [31]X. Li, Z. Li, and J. Yang, *Physical Review Letters* **112**, 018301 (2014).
- [32]K. Zhang, et al., *Nano Letters* **17**, 6676 (2017).
- [33]A.-Y. Lu, et al., *Nat Nano* **12**, 744 (2017).
- [34]W.-J. Yin, B. Wen, G.-Z. Nie, X.-L. Wei, and L.-M. Liu, *Journal of Materials Chemistry C* **6**, 1693 (2018).
- [35]H. C. Yang, J. Hou, V. Chen, and Z. K. Xu, *Angew Chem Int Ed Engl* **55**, 13398 (2016).
- [36]H. U. Din, M. Idrees, A. Albar, M. Shafiq, I. Ahmad, C. V. Nguyen, and B. Amin, *Physical Review B* **100**, 165425 (2019).
- [37]L. Ju, M. Bie, X. Tang, J. Shang, and L. Kou, *ACS Applied Materials & Interfaces* **12**, 29335 (2020).
- [38]L. Zhang, *Journal of Materials Chemistry A* **8**, 8813 (2020).
- [39]A. Rawat, M. K. Mohanta, N. Jena, Dimple, R. Ahammed, and A. De Sarkar, *The Journal of Physical Chemistry C* **124**, 10385 (2020).
- [40]G. Kresse and J. Hafner, *Physical Review B* **47**, 558 (1993).
- [41]G. K. a. J. Furthmuler, *Physical Review B* **54**, 11169 (1996).
- [42]J. Heyd, G. E. Scuseria, and M. Ernzerhof, *The Journal of Chemical Physics* **124**, 219906 (2006).
- [43]S. Grimme, J. Antony, S. Ehrlich, and H. Krieg, *J. Chem. Phys.* **132**, 154104(1) (2010).
- [44]X.-B. Li, P. Guo, Y.-N. Zhang, R.-F. Peng, H. Zhang, and L.-M. Liu, *Journal of Materials Chemistry C* **3**, 6284 (2015).
- [45]S. Bruzzone and G. Fiori, *Applied Physics Letters* **99**, 222108 (2011).
- [46]L. D. Pan, L. Z. Zhang, B. Q. Song, S. X. Du, and H. J. Gao, *Applied Physics Letters* **98**, 173102 (2011).
- [47]Y. W. Son, M. L. Cohen, and S. G. Louie, *Nature* **444**, 347 (2006).
- [48]L. Tapasztó, G. Dobrik, P. Lambin, and L. P. Biró, *Nature Nanotechnology* **3**, 397 (2008).
- [49]Y. Cai, G. Zhang, and Y. W. Zhang, *Journal of the American Chemical Society* **136**, 6269 (2014).
- [50]S. Chen, S. Kim, W. Chen, J. Yuan, R. Bashir, J. Lou, A. M. van der Zande, and W. P. King, *Nano Letters* **19**, 2092 (2019).
- [51]C. Xia, W. Xiong, J. Du, T. Wang, Y. Peng, and J. Li, *Physical Review B* **98**, 165424 (2018).
- [52]M. Q. Long, L. Tang, D. Wang, L. Wang, and Z. Shuai, *Journal of the American Chemical Society* **131**, 17728 (2009).
- [53]J. Bardeen and W. Shockley, *Physical Review* **80**, 72 (1950).
- [54]B. Hou, et al., *The Journal of Physical Chemistry Letters* **11**, 3116 (2020).